Journal of Materials Chemistry A

ROYAL SOCIETY OF CHEMISTRY

PAPER

View Article Online
View Journal | View Issue

Check for updates

Cite this: J. Mater. Chem. A, 2023, 11, 8265

Capillary-induced self-crumpled and sulfur-deficient MoS_2 nanosheets inhibit polysulfide cycling in lithium–sulfur batteries†

Rohan Paste, [abc] Shenghan Li,[c] Jui-Han Fu,[d] Yu-Hsiang Chiang,[e] Arif I. Inamdar, [f] Ming-Hsi Chiang, [f] Vincent Tung,*[de] Hong-Cheu Lin*[abg] and Chih Wei Chu *[chij]

Stable lithium–sulfur batteries (LSBs) have promise to shape a new generation of stable energy-storage devices. Although the energy densities of LSBs (up to 2500 W h kg^{-1}) are higher than those of conventional Li-ion batteries (LIBs), lithium polysulfides (LiPSs) shuttling remains a pressing issue that leads to irreversible loss of active materials, degraded capacity, and eroded durability of LSBs. To tackle this issue, in this study we modified commercial polypropylene (PP) or pristine separators by laminating them with a layer of crumpled MoS_2 (c-MoS_2) nanosheets; the resulting assembly is referred to herein as MC-separator. We synthesized the c-MoS_2 nanosheets using a special electrohydrodynamic process and laminated them onto the PP separator through simple vacuum filtration. The synthesized c-MoS_2 nanosheets featured a metallic 1T-phase enriched with strained sulfur vacancies and a high surface area, providing additional redox reaction sites for LiPSs during battery operations. The c-MoS_2 thin film could adsorb the LiPSs while providing additional reaction sites to reutilize these LiPSs, ultimately enhancing the specific capacity of the battery. When operated at a rate of 0.5C, a cell comprising a sulfur-expanded graphite cathode, the MC separator, and a Li anode provided a high specific capacity (1242 mA h g^{-1}) with approximately 96% coulombic efficiency over 500 cycles. In contrast, a cell prepared with a PP separator, when operated at 0.5C, provided an initial capacity of only 746 mA h g^{-1} and could be run for only 296 cycles. The high capacity and good cycling stability of our new cell indicate that the MC separator could suppress the LiPSs shuttle effect, allowing better utilization of the active materials even at high C rates.

Received 23rd January 2023
Accepted 20th March 2023

DOI: 10.1039/d3ta00411b

rsc.li/materials-a

Published on 29 March 2023. Downloaded on 6/22/2024 6:17:22 AM.

1. Introduction

Lithium–sulfur batteries (LSBs) are promising solutions for future energy storage applications, especially when developing energy-dense Li-metal batteries. Recently, prominent battery development consortiums, including the Battery500, have highlighted the need to achieve a cell-level specific energy density of 500 W h kg^{-1} for application in sustainable electric vehicles (EVs).[1] To this end, the massive theoretical energy density of LSBs (*ca.* 2600 W h kg^{-1}) makes them excellent candidates in the race for high-performance energy-storage devices.[1–3] Notably, this massive energy density is five times higher than that of conventional Li-ion batteries (LIBs), which can offer only 150–250 W h kg^{-1}.[1] The active materials used in LSBs, including sulfur and Li, are abundant and much cheaper than the active materials used in LIBs. LSBs undergo a multi-electron conversion reaction and, thus, offer a high specific capacity of 1675 mA h g^{-1}. Sulfur cathodes also stand out as superior candidates in the cathode race.[4,5] In addition to a high capacity, sulfur provides various other benefits, including non-

[a]Department of Materials Science and Engineering, National Yang Ming Chiao Tung University, 1001 Ta-Hsueh Road, Hsinchu 30010, Taiwan, Republic of China. E-mail: linhc@nycu.edu.tw

[b]Department of Materials Science and Engineering, National Chiao Tung University, 1001 Ta-Hsueh Road, Hsinchu 30010, Taiwan, Republic of China

[c]Research Center for Applied Sciences, Academia Sinica, No. 128, Sec. 2, Academia Road, Nangang, Taipei 11529, Taiwan, Republic of China. E-mail: gchu@gate.sinica.edu.tw

[d]Department of Chemical System Engineering, School of Engineering, The University of Tokyo, Tokyo, Japan. E-mail: vincent@g.ecc.u-tokyo.ac.jp

[e]Physical Sciences and Engineering Division, KAUST Solar Center, King Abdullah University of Science and Technology (KAUST), Thuwal, Saudi Arabia

[f]Institute of Chemistry, Academia Sinica, No. 128, Sec. 2, Academia Road, Nangang, Taipei 11529, Taiwan, Republic of China

[g]Center for Emergent Functional Matter Science, National Yang Ming Chiao Tung University, 1001 Ta-Hsueh Road, Hsinchu 30010, Taiwan, Republic of China

[h]College of Engineering, Chang Gung University, Taoyuan City 33302, Taiwan, Republic of China

[i]Center for Green Technology, Chang Gung University, Taoyuan City 33302, Taiwan, Republic of China

[j]Department of Photonics, National Yang Ming Chiao Tung University, 1001 Ta-Hsueh Road, Hsinchu 30010, Taiwan, Republic of China

† Electronic supplementary information (ESI) available. See DOI: https://doi.org/10.1039/d3ta00411b

Published on 29 March 2023. Downloaded on 6/22/2024 6:17:22 AM.

toxicity, high energy density, and low material cost.[6] Nevertheless, sulfur cathodes have yet to be accepted for commercial applications because of (i) the huge volume change that occurs during cycling of the battery, (ii) the insulating nature of sulfur and its discharged products (Li_2S_2/Li_2S), causing a high redox overpotential, and (iii) decomposition of their electrolytes, due to insoluble LiPSs, interface destabilization, and loss of active materials. The volume expansion of a sulfur cathode is more significant during the cycling process. Upon reduction, the sulfur atoms are converted to Li_2S, which has a lower density (*ca.* 1.66 g cm^{-3}) than that of pure sulfur (2.03 g cm^{-3}); this fully converted Li_2S can expand by as much as 80%, potentially pulverizing the cathode.[7] The large redox overpotential is due to the diffusion of polysulfides inducing the passivation of active electrodes; continuous redox consumption of active electrode materials can result in the loss of electronic contact with a three-dimensional (3D) conductive matrix and formation of inactive sulfur in the cathode.[8] The presence of sulfur and the discharged products such as Li_2S_2 and Li_2S can result in low utilization of active materials in a cell.[9] The ready dissolution of LiPSs leads to a "polysulfide shuttle" between the cathode and anode, increasing the charging time of the cell toward infinity and hampering the stability, coulombic efficiency (CE), and lifetime of the battery.[5,10,11] Among these drawbacks, the shuttling of soluble LiPSs (Li_2S_x, $4 < x < 8$) between the cathode and anode is a grave issue that can diminish the electrochemical performance and cycling stability of LSBs.[2,12,13]

Several strategies have been investigated to eradicate the shuttling of LiPSs, including the use of nanomaterials as sulfur hosts,[14,15] composite sulfur cathodes with alkali metals,[16] multifunctional binders to immobilize the LiPS,[11,17,18] electrolyte engineering with additives,[4,19] and modification of the separator and interface engineering.[20–22] Among these approaches, modification of the separator has been the most effective, although it remains a challenge to enhance the utilization of LiPSs. A separator is a key part of a battery; it maintains the diffusion of Li^+ ions and avoids direct contact between the anode and cathode. Initial studies on the modification of separators revealed that nanoporous separators could provide sufficient room for the production of LiPSs.[12,13] During charge/discharge cycling, these LiPSs can precipitate onto the cathode (*i.e.*, the nearest conductive surface) or shuttle between the anode and cathode. Hence, a conducting interlayer with a large surface area can facilitate the reutilization of LiPSs during charge/discharge cycles. In recent years, several metal oxides and dichalcogenides have been used to modify PP separators to mitigate the shuttling of LiPSs, including an interlayer of MoO_3 with carbon nanotubes,[23] self-assembled MnO_2,[24] Ni/SiO_2 mixed with graphene,[24] CeO_2 nanocrystals modified with carbon nanofibers,[20] and MoS_2 bulk particles/nanosheets.[25–27] Nevertheless, rapid capacity decay and poor cycling stability remain formidable challenges when using these modified separators.

In this paper, we report the use of rationally designed crumpled MoS_2 (c-MoS_2) nanosheets as a polysulfide barrier on the Celgard-2500/PP separator. We used an electrohydrodynamic (EHD) process to induce a dimensional transformation of two-dimensional (2D) planar MoS_2 sheets into the crumpled and structurally deformed 3D c-MoS_2 nanosheets.[28,29] Compositionally engineered 3D/3D homo- and heterostructures can be patterned selectively into mechanically strong, radiation tolerant and electrochemically active layers, potentially putting an end to polysulfide migration in LSBs, while also enhancing battery performance. Interestingly, we found that the additional electronic conductivity, high electrochemically active surface area (EASA), and strained sulfur vacancies on the c-MoS_2 surface boosted the utilization of sulfur and LiPSs. In particular, during the chemical exfoliation and EHD process, the conversion of the semiconducting 2H phase to the metallic 1T phase of the c-MoS_2 nanosheets contributed additional electronic conductivity for lamination of the c-MoS_2 nanosheets on the PP separator, forming an assembly referred to herein as an "MC-separator". This 1T phase of the c-MoS_2 nanosheets helped to decrease the internal resistance of the cell and revamp the charge conduction in the battery. As a result, an LSB prepared with the MC separator exhibited an initial capacity of 1242 mA h g^{-1} when operated at a rate of 0.5C (1C = 1600 mA h g^{-1}) with 96% CE over 500 cycles. The capacity retention between the 100th and 200th cycles was 95.7%, whereas it was approximately 85% between the 50th and 500th cycles. At a higher rate of 5C, the same separator provided an initial capacity of 709 mA h g^{-1} with 88% CE over 1800 cycles.

2. Experimental procedures

2.1 Chemically exfoliated MoS_2 (ce-MoS_2)

A modified version of a previously reported method for Li intercalation was employed.[28] MoS_2 bulk powder (1 g) was submerged in 1.6 M *n*-butyllithium in hexane (15 mL) and stirred vigorously for at least 96 h in an Ar-filled glove box. The mixture was then filtered using Whatman filter paper, washed several times with hexane, and removed from the glove box. The intercalated MoS_2 compound was placed in deionized water (DI-H_2O, 100 mL) and sonicated for 2 h to accomplish exfoliation.

2.2 3D c-MoS_2

A stable dispersion of 2D exfoliated MoS_2 sheets was mixed with isopropyl alcohol (IPA) in a volume ratio of 1 : 3. The MoS_2 ink solution (250 μg mL^{-1}) was fed into a needle (gauge 18 TW) by a programmable syringe pump at a flow rate of 5 μL min^{-1}. An external electric field (1.35 kV cm^{-1}) was generated on the needle by a high-voltage power supply (ES 40P-20 W/DAM, Gamma High Voltage Research) with a spraying distance of 5 cm between the needle tip and the Si wafer substrate. The humidity was set in the range 35–40% to maintain the evaporation rate. The deposited powder on the Si substrate was collected by scraping to achieve a high yield (*ca.* 97%) of the 3D c-MoS_2.

2.3 c-MoS_2/PP separator (MC separator)

The as-prepared c-MoS_2 powder was redispersed in IPA and homogenized with ultrasonication. The c-MoS_2 nanosheets were laminated onto a PP separator through simple vacuum-

 This journal is © The Royal Society of Chemistry 2023

Published on 29 March 2023. Downloaded on 6/22/2024 6:17:22 AM.

filtration. After filtering the mixture of c-MoS_2 and IPA onto a conventional Celgard-2500 separator/PP separator, a compact, thin layer of c-MoS_2 was formed on top. The crumpled structure of c-MoS_2 became interlocked on the porous PP separator, which exhibited superior adhesion to the c-MoS_2 nanosheets. The MC separator was dried in a vacuum oven at 50 °C for 24 h and then cut into circular pieces for battery fabrication.

2.4 Cathode

For electrochemical testing, a sulfur-expanded graphite (SEG) cathode was prepared using a previously reported procedure.[30] The SEG containing 20 wt% EG and 80 wt% sulfur was mixed with carbon black (Super-P) and poly(vinylidene difluoride) (PVDF) (ratio: 70 : 20 : 10 wt%) in a suitable amount of *N*-methyl-2-pyrrolidone (NMP). The mixture was ball milled for 3 h. The as-obtained homogeneous slurry was blade-coated onto aluminum (Al) foil, using a 300 μm-thick blade coater, and dried at 50 °C for 12 h. The obtained cathode was cut into a small disc with an average sulfur loading of 1.5–2 mg cm^{-2}.

2.5 Cell assembly

CR-2032 coin cells were assembled using SEG as the cathode, an MC or PP separator, and Li foil as the anode. The cells were assembled with an electrolyte [1 M LiTFSI and $LiNO_3$ (1 wt%) in 1,2-dioxolane (DOL)/dimethoxyethane (DME) (1 : 1, v/v); 40 μL] in an Ar-filled glove box (O_2 and H_2O levels: <0.1 ppm). Stainless steel (SS) plate was as an electrode in the fabrication of the SS‖separator‖SS cell to calculate the surface resistance.

2.6 LiPSs solution

A LiPSs solution was prepared from Li_2S_6 using a previously reported procedure.[31] S_8 and Li_2S (molar ratio: 5 : 8) were dissolved in DOL/DME (1 : 1) and stirred overnight at 60 °C to provide a dark-yellow solution of Li_2S_6.

2.7 Characterization

X-ray diffraction (XRD) patterns were recorded using an X-ray diffractometer (X'Pert3 Powder, PAN analytical) within angles 2θ ranging from 10 to 80°. Scanning electron microscopy [SEM, FEI Nova scanning electron microscope (2–10 kV)] was used to observe the morphologies of the separator and Li-metal anode. The cycled Li anode and separators were washed with DOL/DME (1 : 1) and dried for 24 h. To avoid contamination or degradation, the samples were transferred to the SEM chamber with gas sealing. X-ray photoelectron spectroscopy (XPS, PHI 5000 Versa Probe) with an Al (Kα) X-ray source (1486.6 eV) was used for post-cycling analysis of the separators. Transmission electron microscopy (TEM, JEOL JEM-ARM300F2), with double spherical aberration correctors operated at 300 kV, was used to study the crystal structures of MoS_2 and c-MoS_2; the probe size was 0.6 Å, the convergence angle was 24 mrad, and the current was 46 pA. An annular detector having a collection range of 64–180 mrad was used. The size of the high-angle annular dark field (HAADF) images was 1024 × 1024 pixels, captured within 32 s. Absorption spectra of LiPSs solutions were recorded using a Jacob V-670 UV-vis spectrometer. The surface area and pore size distribution of the samples were measured by Micromeritics 3Flex Surface and Catalyst Characterization Analyzer at 77 K under nitrogen (N_2).

2.8 Electrochemical measurements

Cyclic voltammetry (CV) of Li–S cell was performed in the potential range from 1.5 to 3.0 V at a scan rate of 0.1 mV s^{-1}, using an Autolab PGSTAT302N instrument. Electrochemical impedance spectroscopy (EIS) was performed in the frequency range from 0.1 MHz to 0.1 Hz (amplitude: 10 mV) by using an Autolab PGSTAT302N instrument. Galvanostatic charge/discharge (GCD) profiles and electrochemical performance data were recorded using a battery testing system (AcuTech Systems, Taiwan). The operating voltage window for the Li–S cell was set from 1.5 to 3.0 V; the cell was operated at various C-rates (1C = 1600 mA h g^{-1}). Origin 2018 was utilized to plot and process the obtained data.

3. Results and discussion

The c-MoS_2 nanosheets were obtained through a new method in which chemically exfoliated MoS_2 (ce-MoS_2) separated into layers and then modified into crumpled structures. The dimensional transformation of the 2D ce-MoS_2 sheets to crumpled and structurally deformed 3D c-MoS_2 nanosheets was achieved using an EHD process.[28,29] The as-modified c-MoS_2 nanosheets were enriched with strained-sulfur vacancies, featured a high EASA, and displayed the 1T phase of MoS_2 (Scheme 1). We laminated the c-MoS_2 onto a PP separator through simple vacuum-filtration with the goal of achieving LiPSs inhibition in LSBs. The highly porous structure and larger surface area of the c-MoS_2 can accommodate the LiPSs and provide additional reaction sites for LiPSs during cell operation. Additionally, the S-vacancies and unique physical structure of c-MoS_2 with several edges and ridges may help to adsorb LiPSs which prevents the migration of LiPSs and promotes their utilization during cycling. After applying an electric field (1.35 kV cm^{-1}), the single-layered ce-MoS_2 (Fig. 1a) was converted into a crumpled structure; high-resolution transmission electron microscopy (HRTEM) exposed the basal plane of ce-MoS_2, revealing an internal edge-like structure (Fig. 1b). The TEM images in Fig. 1c and d reveal that the structure of c-MoS_2 featured many corrugated edges, wrinkles, and ridges. In contrast, the TEM images of commercial MoS_2 and ce-MoS_2 revealed flat surface morphologies without any corrugated edges or wrinkles (Fig. S1a and b†). XRD patterns confirmed the crystalline structure and phase change of MoS_2 (Fig. S2†). The pattern of the commercial MoS_2 provided peaks representing the 2H-MoS_2 phase (JCPDS #37-1492) without any crystalline impurities, consistent with previous reports.[32,33] The peaks at values of 2θ of 14.19, 32.52 to 35.75, 39.41, 49.68, 58.39, and 60.15° represented the (002), (100) to (101), (103), (105), (110), and (201) planes, respectively, of 2H-MoS_2.[32] In contrast, the XRD pattern of the c-MoS_2 nanosheets featured a shifting of some peaks, especially the (002), (110), and (201) peaks, and the

Published on 29 March 2023. Downloaded on 6/22/2024 6:17:22 AM.

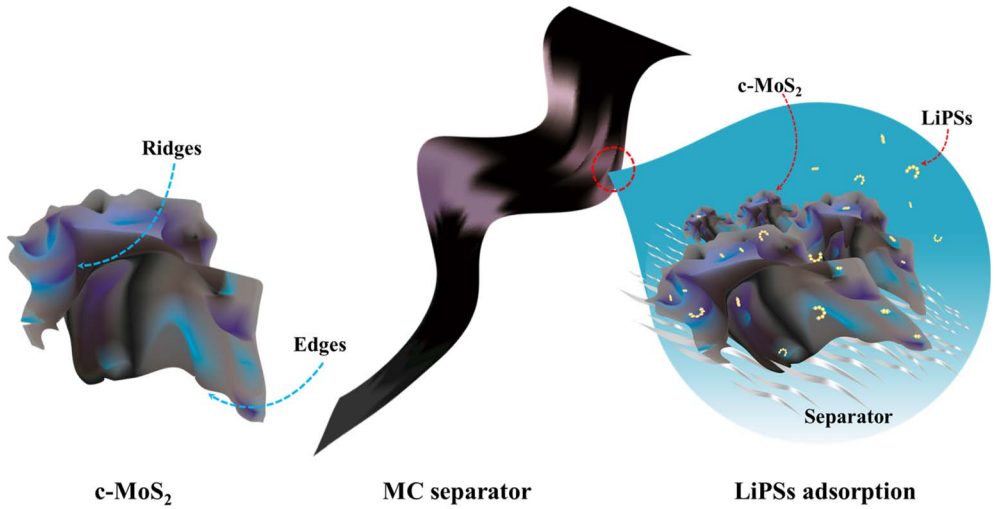

Scheme 1 Schematic representations of the structure of c-MoS_2, the MC separator, and the adsorption of LiPSs on the corrugated edges and ridges.

absence of the (103) peak. This shift in the values of 2θ and the absence of some peaks suggested the conversion of 2H-MoS_2 to 1T-MoS_2, as has been reported previously.[34,35] The smaller and broader peaks of c-MoS_2 suggested the presence of smaller-dimension c-MoS_2 nanosheets. The absence of some signals might have been relate to the structural defects in the c-MoS_2 structure.[36] We employed these unique c-MoS_2 structures for LiPSs suppression in LSBs. The c-MoS_2 nanosheets had a larger fraction of the 1T-phase (*ca.* 65%), as we have stated previously.[29] The presence of the 1T phase would provide certain benefits to the MC separator. For example, the c-MoS_2 would have additional electronic conductivity that could decrease the interfacial resistance.[37] Moreover, the metallic nature of 1T-MoS_2 could improve the charge transfer rate, potentially beneficial for electrochemical applications.[38] The XPS spectra of the commercial MoS_2 and c-MoS_2 nanosheets revealed a change in phase of the two materials. After the structural transformation, the c-MoS_2 nanosheets exhibited the 1T phase (Fig. 1e). The spectrum of the commercial MoS_2 featured peaks at 228.19 and 231.32 eV, corresponding to Mo $3d_{5/2}$ and Mo $3d_{3/2}$, respectively.

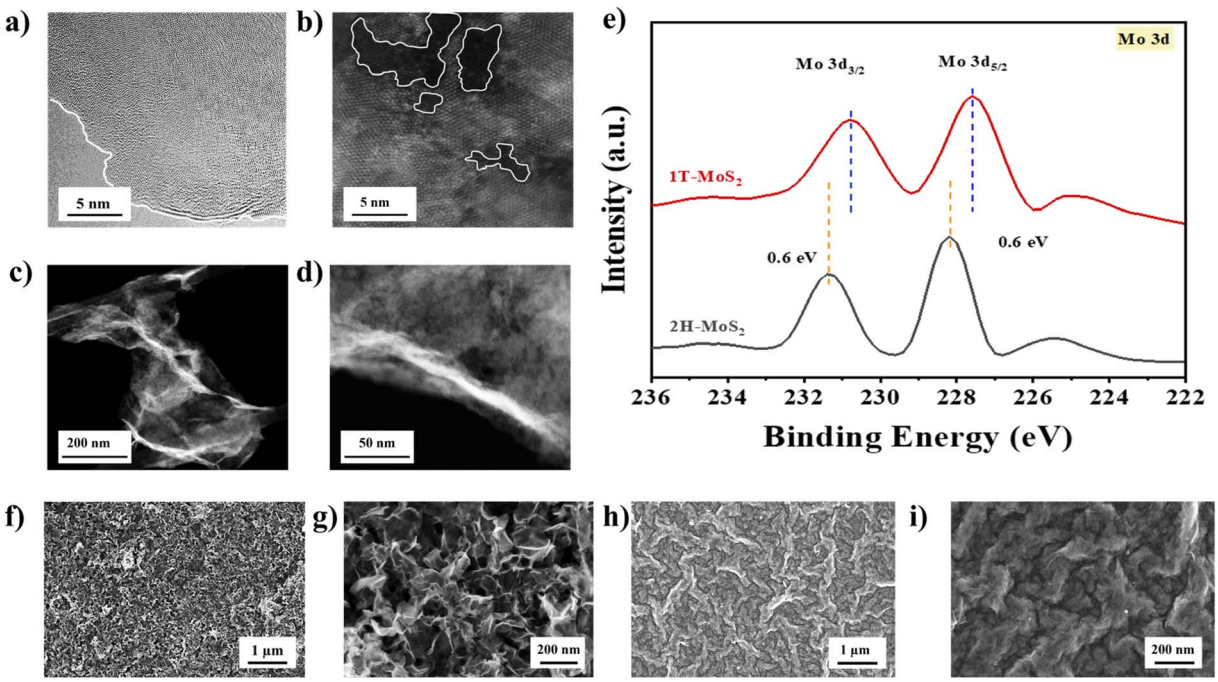

Fig. 1 (a and b) HRTEM images of ce-MoS_2, revealing (a) a single layer and (b) its internal edges. (c and d) TEM images of c-MoS_2, revealing (c) its crumpled structure and corrugated edges and (d) an edge of the c-MoS_2 structure. (e) XPS spectra of the 2H- and 1T-MoS_2 phases. (f–i) SEM images of (f and g) c-MoS_2 and (h and i) ce-MoS_2 nanosheets.

 This journal is © The Royal Society of Chemistry 2023

Published on 29 March 2023. Downloaded on 6/22/2024 6:17:22 AM.

In the spectrum of c-MoS_2, these peaks had shifted by 0.6 eV toward lower binding energies, indicative of the structural change in the c-MoS_2. In addition, N_2 adsorption and pore size distribution studies were carried out for commercial MoS_2 and modified c-MoS_2 to determine the surface area. The results indicate that c-MoS_2 has a higher surface area of 36.59 $m^2\ g^{-1}$ as compared with 6.19 $m^2\ g^{-1}$ for the commercial MoS_2 (Fig. S3a and b†). This incremental surface area of c-MoS_2 enhances the solid–liquid contact which allows easier deposition of LiPSs and inhibits their shuttling.[39] Inset figure in Fig. S3a and b† showed the pore size distribution $dv/d\log(D)$ pore volume ($cm^3\ g^{-1}$) V_s pore diameter for c-MoS_2 and commercial MoS_2 which is around 3.2–3.8 nm.

To prepare the modified separator, c-MoS_2 powder (2 mg) was dispersed in IPA (10 mL) and vacuum-filtered onto a PP separator. We suspected that the c-MoS_2 would become interlocked within the porous structure of the PP separator, due to the inward force during the vacuum-filtration process (Scheme S1†). The many corrugated edges and ridges would facilitate the c-MoS_2 to adsorb LiPSs during cycling. The SEM images in Fig. 1f and g reveal a highly porous structure of c-MoS_2 on the PP separator that would likely be effective for the trapping of LiPSs and their possible reutilization during cell cycling. The crumpled structure of c-MoS_2 adhered well to the PP separator, potentially beneficial for achieving an effective interlayer. In contrast, the flat and nonporous structure of ce-MoS_2 on the PP separator would not be beneficial for LiPSs adsorption (Fig. 1h and i). The commercial MoS_2 existed in the form of large chunks that could readily become detached, making them inappropriate for use as an inhibition layer to mitigate the shuttling of LiPSs (Fig. S4a and b†). The cross-sectional SEM image in Fig. 2a reveals that the use of 2 mg of c-MoS_2 produced a 4.6 μm-thick layer of c-MoS_2 on the PP separator. The use of 2 mg of c-MoS_2 in the solution provided an average loading of 0.12 mg cm^{-2} on each PP separator. The dispersion of c-MoS_2 of 2 mg was suitable for forming a shielding layer for LiPSs. A lower amount of c-MoS_2 (~1 mg) was not sufficient to form a regular lamination on the PP separator (Fig. S5a†). Whereas a greater amount of c-MoS_2 cause increased resistance in the cell. Based on the EIS study of SS||separator||SS cells, it was confirmed that the surface resistance of 2.2, 7.2, 9.6, and 15.8 Ω was recorded for PP separator, MC separator with 2 mg, 5 mg, and 10 mg dispersion respectively (Fig. S5b†). The higher amount of loading can affect the porosity of the coated layer and electrolyte uptake which can lead to heightened resistance at the interface between the cathode and separator, potentially deteriorating the battery performance.[40] The performance of the MC separator prepared with a higher amount of c-MoS_2 (5 mg and 10 mg) has been studied in comparison to 2 mg dispersion. A tape adhesion test revealed that the c-MoS_2 was undetachable from the PP separator; in contrast, the commercial MoS_2 and ce-MoS_2 readily became stuck on the gummed side of the tape, confirming its poor adhesivity (Fig. S6a–c†). A folding recovery test affirmed the flexibility of the MC separator and the adhesivity of c-MoS_2 on the PP separator (Fig. 2b).

The LiPSs migration through the separator was observed using a symmetrical H-cell, with the right column filled with Li_2S_6 solution and the left column filled with blank electrolyte solution. The two sides were separated by either a PP separator or an MC separator. Fig. 2c reveals that the MC separator effectively prevented the migration of LiPSs. After 5 h, a trace amount of LiPSs appeared to be infiltrated into the blank electrolyte, presumably due to initial impregnating of the LiPSs into the dense c-MoS_2 structure. After 24 h, no further infiltration of LiPSs had occurred, confirming that the LiPSs had adsorbed on the surface of the MC separator. The stronger adsorption effect induced by the nanoporous structure of c-MoS_2 helped to reutilize the active materials by mitigating the LiPSs shuttle mechanism.[13] In contrast, the PP separator readily allowed (within 10 h) the LiPS species to enter into the blank electrolyte solution. The blank electrolyte changed from pale yellow to dark brown within 24 h, indicating that LiPSs migration had occurred in the presence of the PP separator. These observations suggest that the c-MoS_2 nanosheets could adsorb the LiPSs, thereby suppressing the migration of Li_2S_6 and further battery degradation. Fig. 2d displays the UV-vis absorption spectrum recorded after the filtered solution had been aging for 24 h. The absorbance intensity was measured in the range from 350 to 800 nm. The normal LiPSs solution featured a strong absorbance in the range 380–500 nm.[41] Because the LiPSs solution readily passed through the PP separator, its absorbance was similar to that of the normal solution of LiPSs. In contrast, the MC separator did not allow passage of these LiPSs to the other side of the H-cell, resulting in a clearer solution with low visible absorption, indicative of a lower degree of migration of the LiPSs and, hence, a higher degree of adsorbability of the LiPSs on the c-MoS_2 nanosheets.

Polysulfide migration not only decreases the amount of active material but also affects the morphology of the Li anode surface. Upon continuous LiPSs shuttling, a Li anode will undergo surface degradation through LiPSs attack (Fig. 2e). These nonconductive and insoluble deposits of LiPS species on the Li metal anode result in an inactive surface layer, which leads to failure of the cell.[42,43] After 25 charge/discharge cycles, we disassembled the cells incorporating the MC and PP separators to observe (SEM) the morphologies of their Li anodes. The Li anode assembled with the MC separator exhibited minor surface degradation, suggesting that the MC separator suppressed LiPSs migration and led to uniform Li^+ ion deposition (Fig. 3a and b). The nanoporous structure of c-MoS_2 accommodated and reutilized the LiPS on the cathode side, resulting in enhanced cell capacity. The suppressed LiPSs shuttling indirectly assisted the health of the Li metal anode. We attribute the superior battery performance to the suppressed LiPSs migration and stable Li anode surface. In contrast, massive degradation occurred to the Li anode in the cell prepared with the PP separator (Fig. 3c and d). This Li anode surface featured enormous degrees of growth of Li dendrites and etching. Such severe degradation would likely cause the loss of active Li through continuous breakdown of the solid electrolyte interphase (SEI), ultimately compromising the battery's capacity and stability.[44] Moreover, the continuous growth of Li dendrites could lead to penetration through the separator, resulting in

Published on 29 March 2023. Downloaded on 6/22/2024 6:17:22 AM.

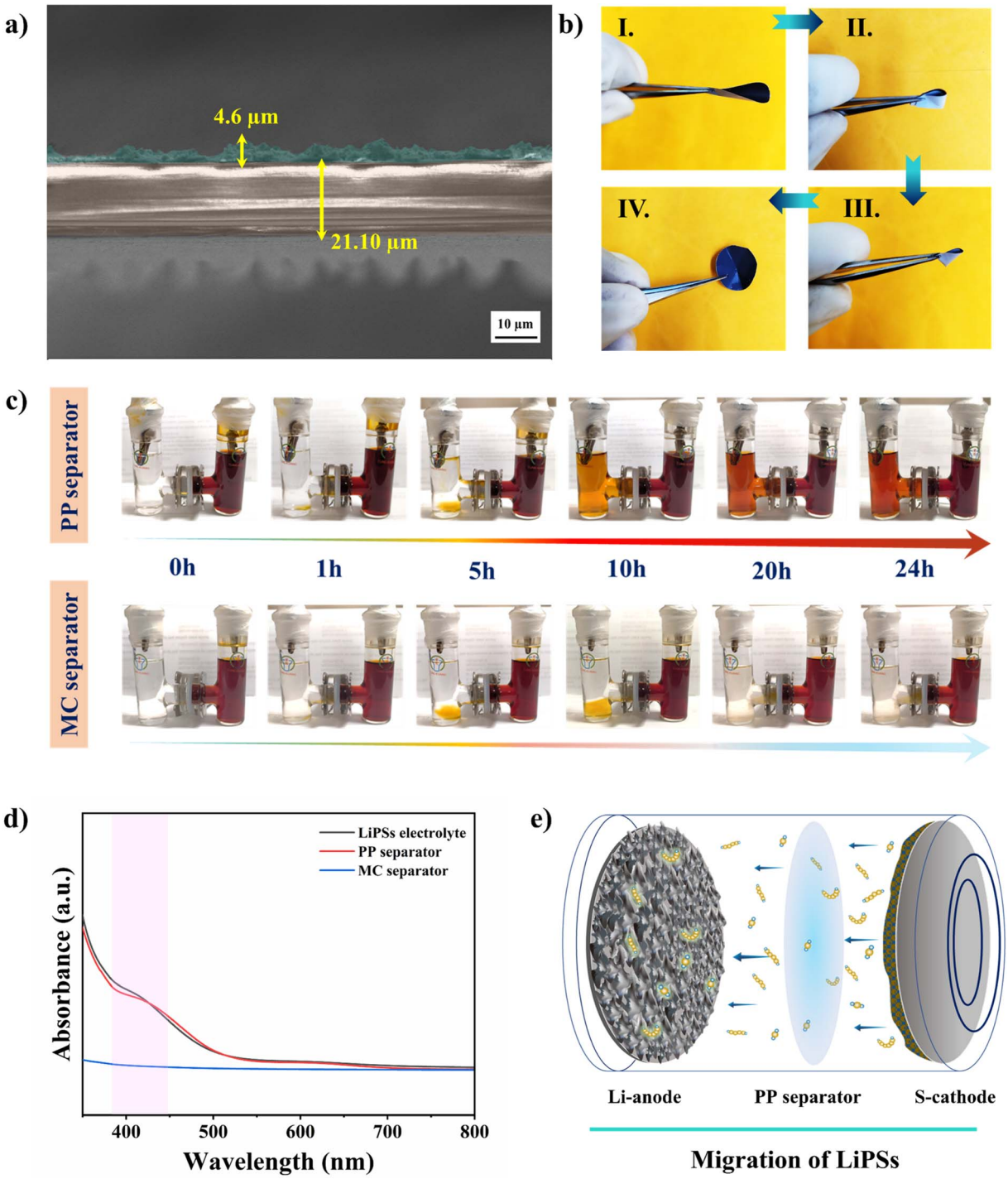

Fig. 2 (a) Cross-sectional SEM image of the MC separator, revealing the thicknesses of the c-MoS_2 layer and PP separator. (b) Folding recovery test of the MC separator. (c) Shuttling mechanism of LiPSs, determined using H-cells. (d) UV-vis spectra of LiPS solutions passed through PP and MC separators. (e) Schematic representation of LiPSs and the degradation of electrodes in an LSB prepared with a PP separator.

internal short circuits and potential fire accidents.[4] Hence, the stability of the Li metal also plays a vital role in LSB operation.

Next, we used SEM to analyze the surfaces of the MC and PP separators to study the migration of the LiPSs during the charge/discharge cycles. We cycled the cells for 20 cycles at a rate of 0.5C and then dissembled them to observe the surfaces of the separators. During cell operation, LiPSs can accumulate within the porous structure of the separator and form layers on both sides. Fig. S7† reveals the difference between the cathode- and anode-facing sides of the MC separator. The cathode-facing side (*i.e.*, the c-MoS_2-coated side) revealed the presence of a c-MoS_2 layer and some deposition or agglomerates of LiPSs upon

 This journal is © The Royal Society of Chemistry 2023

Published on 29 March 2023. Downloaded on 6/22/2024 6:17:22 AM.

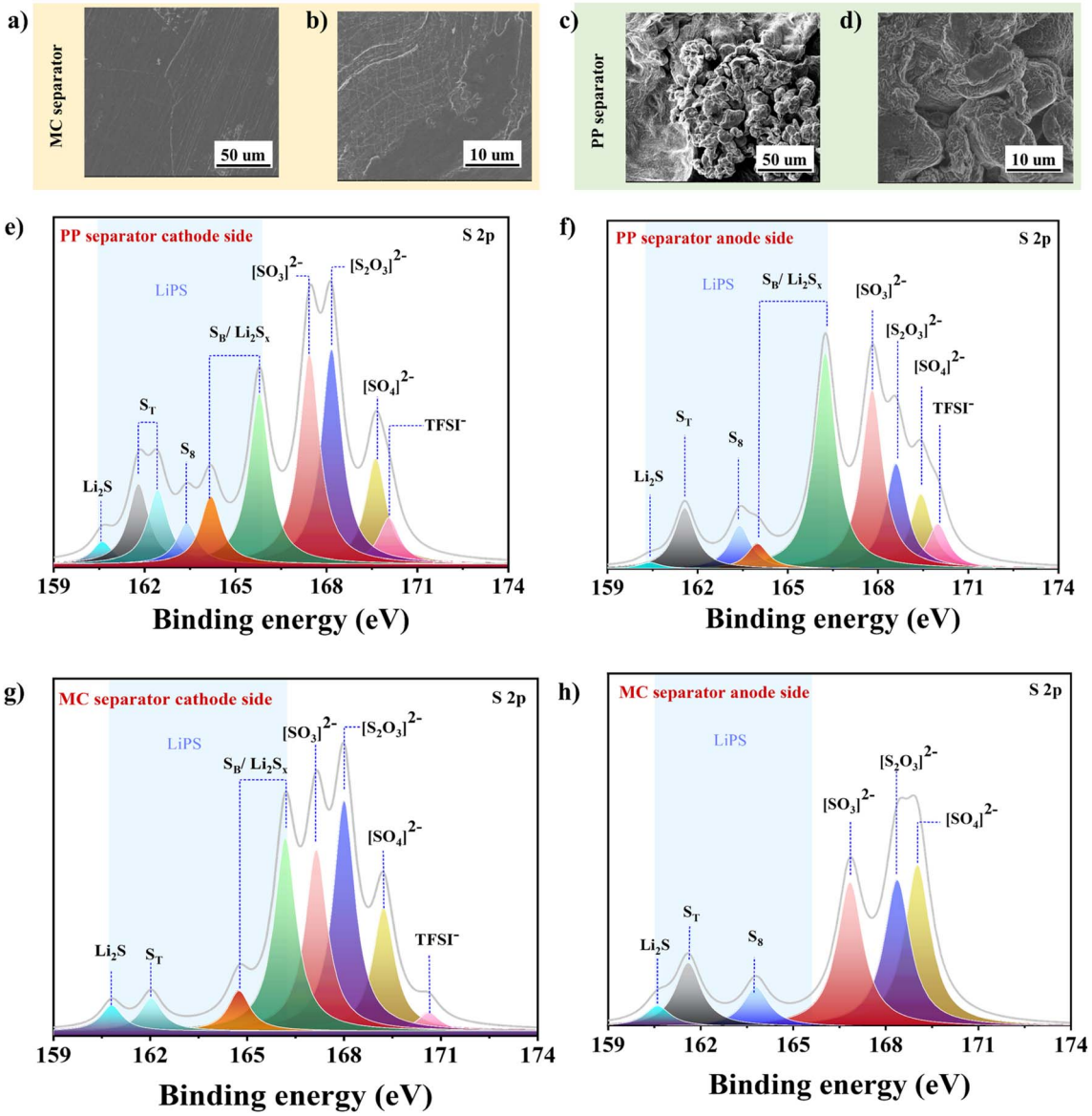

Fig. 3 (a–d) SEM images of Li anode surfaces before and after 25 cycles, with (a and b) MC and (c and d) PP separators. (e–h) XPS spectra of the cathode- and anode-facing sides of (e and f) PP and (g and h) MC separators.

it. In contrast, the anode-facing side of the MC separator (*i.e.*, the side absent of c-MoS_2) revealed the porous pattern of the separator. This pattern indicates that regular charge transfer had occurred through the MC separator without any abnormal growth on the anode side. In contrast, both the cathode- and anode-facing sides of the PP separator featured massive depositions or agglomerates of LiPSs (Fig. S7†), suggesting that the PP separator could not prevent the migration of LiPSs from the cathode to the anode side. It readily allowed the LiPSs to pass through, triggering degradation of the Li anode.[20] These observations are consistent with the SEM images of the Li metal anodes assembled with the MC and PP separators, and confirms the ability of the MC separator to prevent the migration of LiPSs in the LSBs.

We also used XPS for post-cycling analysis of both separators after cycling them for 50 cycles at a rate of 0.5C. We analyzed the surfaces of the separator facing the cathode and anode to detect the trapped LiPSs. Signals for several LiPS species were evident on the PP separator surface facing the cathode side (Fig. 3e) at 160.05, 161.80/162.38, 163.36, 164.17, and 165.77 eV representing Li_2S, terminal sulfur (S_T) in Li_2S_x, elemental sulfur (S_8), bridging sulfur (S_B), and Li_2S_x species, respectively. Furthermore, signals appeared at 167.41, 168.14, 169.67, and 170.07 eV for sulfite (SO_3^{2-}), thiosulfate ($S_2O_3^{2-}$), sulfate (SO_4^{2-}), and $TFSI^-$ anions, respectively.[45–47] Fig. 3f presents the XPS spectrum of the PP separator facing the anode side. Surprisingly, an intense signal for Li_2S_x appeared at 166.24 eV, confirming the huge migration of LiPSs.[17] In the case of the MC separator, the XPS spectrum of the side facing the cathode featured several

Published on 29 March 2023. Downloaded on 6/22/2024 6:17:22 AM.

peaks for long- and short-range LiPSs, mainly at 160.7, 162, 164.7, and 166.18 eV, which we assign to Li_2S, S_T, S_B, and Li_2S_x species, respectively (Fig. 3g). In detail the content of Li_2S (160.7 eV) on the cathode side of the MC separator is higher than the cathode side with PP separator (160.05 eV). This indicates the possible conversion of long-range LiPSs to short-range LiPSs with the help of an MC separator. The XPS spectrum of the side of the MC separator facing the anode contained fewer peaks, mainly associated with Li_2S, S_T, and S_8 species at 160.59, 161.58, and 163.75 eV respectively (Fig. 3h). The spectrum of the anode side of the MC separator featured a tiny peak for Li_2S and precise peaks for S_T and S_8, indicating that small amount of LiPSs had migrated through the MC separator or had undergone conversion on the anode side. This analysis confirms that the MC separator aided in the suppression of LiPSs shuttling, as well as the possible reutilization, followed by adsorption, of the LiPSs on the c-MoS_2 nanoporous structure.

We recorded EIS spectra of the LSBs containing the MC and PP separators to examine the impedance of the cells before and after 20 cycles (Fig. 4a and b). We fitted the EIS spectra recorded for the MC and PP separators prior to cycling with an equivalent circuit (Fig. S8†), where R_0 is the interfacial contact resistance of the electrolyte and cell, $R_{sf\text{-}1}$ and $R_{sf\text{-}2}$ are the surface film resistances, and R_{ct} is the charge transfer resistance.[25] Here, $R_{sf\text{-}1}$ is the resistance caused by the insulating layer of short-range LiPSs between the separator and cathode, and $R_{sf\text{-}2}$ is the resistance due to the formation of an insulating layer on the Li anode as a result of the diffusion of LiPSs. The value of R_{ct} of the PP separator increased dramatically from 14.15 Ω prior to cycling to 64.62 Ω after the 20 cycles (Fig. 4a); for the MC separator, it decreased from 86.1 to 7.72 Ω (Fig. 4b), consistent with the c-MoS_2 interlayer on the PP separator inhibiting the migration of LiPSs, forming a stable SEI, and regulating the Li^+ ion pathways. The resistances related to the PP separator increased (Table S1†) after cycling, consistent with the degradation of the Li anode and sulfur cathode surfaces, due to the diffusion of LiPSs, and eventual generation of insulating layers upon the separator. These findings are in good agreement with the SEM images of the anodes (Fig. 3a–d) and separators (Fig. S7†) before and after cycling.

We performed CV of the LSBs containing the MC and PP separators to examine the transformations of sulfur to Li_2S and *vice versa*. These CV were recorded at a scan rate of 0.05 mV s^{-1}. The CV curves of the MC separator remained almost overlapped for three consecutive cycles, indicating the efficient reversibility of the sulfur redox reactions (Fig. 4c). The changes in the peak potential were minimal, suggesting amelioration of the LiPSs utilization in the cell.[48] The first reduction peak (cathodic reaction) at 2.31 V (*vs.* Li^+/Li) implied the following conversion reactions:

$$S_8 + 2e^- + 2Li^+ \rightarrow Li_2S_8 \quad (1)$$

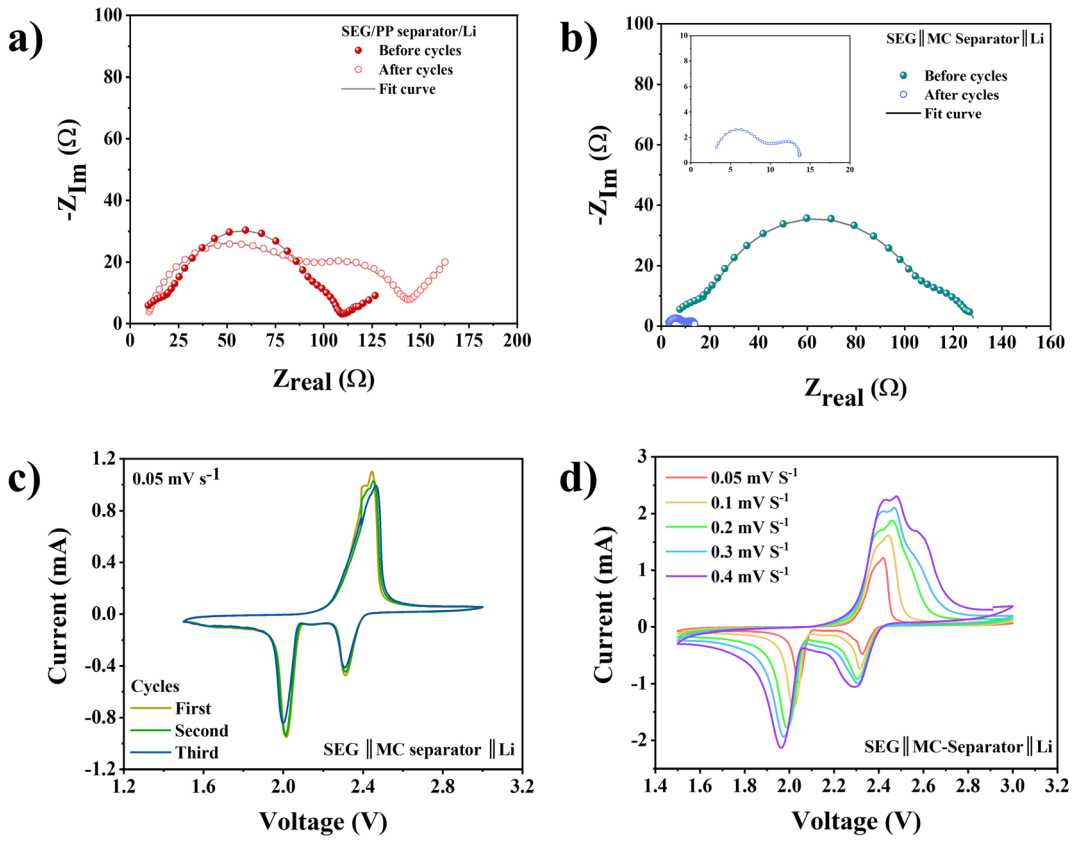

Fig. 4 (a and b) EIS spectra of LSBs recorded before and after 20 cycles with (a) PP and (b) MC separators. (c) CV profiles of an LSB incorporating an MC separator, recorded at a scan rate of 0.05 mV s^{-1}. (d) CV profiles of an LSB incorporating an MC separator, recorded at various scan rates.

 This journal is © The Royal Society of Chemistry 2023

Published on 29 March 2023. Downloaded on 6/22/2024 6:17:22 AM.

$$3Li_2S_8 + 2e^- + 2Li^+ \rightarrow 4Li_2S_6 \quad (2)$$

$$2Li_2S_6 + 2e^- + 2Li^+ \rightarrow 3Li_2S_4 \quad (3)$$

Further reduction of the LiPS species was evidenced by the second reduction peak at 2.0 V (*vs.* Li^+/Li), representing the following reactions:

$$Li_2S_4 + 2e^- + 2Li^+ \rightarrow 2Li_2S_2 \quad (4)$$

$$Li_2S_2 + 2e^- + 2Li^+ \rightarrow 2Li_2S \quad (5)$$

During the anodic scan, one sharp oxidation peak with a minor subpeak was evident at 2.44 V (*vs.* Li^+/Li), attributable to the oxidation of Li_2S_2/Li_2S to S_8. In contrast, the CV curves of the cell prepared with a PP separator featured irregular oxidation and reduction peaks with a drastic decrease in peak current density (Fig. S9†). The peak potentials of the reduction peaks shifted to more negative values, while those peak in the oxidation curve shifted to positive values, indicative of the insufficient conversion of LiPSs.[14] The CV curves were also irregular and did not overlap with one another, suggesting poor reaction kinetics due to insufficient polysulfide conversion.

We investigated the reaction kinetics in the LSB with the MC separator through CV at various scan rates in the range from 0.05 to 0.4 mV s^{-1} (Fig. 4d). The peak current density of the oxidation and reduction peaks increased upon increasing the scan rate, without any abnormalities. The well-shaped CV peaks suggested good electrochemical stability, decreased degradation of the electrodes, a lower degree of LiPSs shuttling, and enhanced reaction kinetics in the cell containing the MC separator.[20]

To check the compatibility of the MC separator, we applied it in a coin cell containing Li metal foil as the anode and SEG as the cathode. We expected the LSB with the MC separator to exhibit superior performance, due to mitigated migration of the LiPSs and the benefits of the c-MoS_2 structure (Scheme 1). We cycled the coin cells at various C-rates. At 0.5C (1C = 1600 mA h g^{-1}), the cell containing the MC separator exhibited stable electrochemical performance, with an initial capacity of 1242 mA h g^{-1}, a capacity of 651 mA h g^{-1} after 500 cycles, and 96% CE (Fig. 5a). The capacity decreased during the initial 20 cycles, but remained stable thereafter for up to 500 cycles. This trend suggests that LiPSs were generated during the initial cycles, and that they remained trapped within the confined interfacial area of the MC separator and cathode. These polysulfides were presumably reutilized during the further charge/discharge cycles, reflected by the stabilized battery performance.[49] The capacity retention between the 100^{th} and 200^{th} cycles was 95.7%, whereas it was approximately 85% between the 50^{th} and 500^{th} cycles. The decay rate between the 100^{th} and 200^{th} cycles was approximately 0.043% per cycle. In contrast, the cell containing the PP separator provided a lower initial capacity (746 mA h g^{-1}) and could be run for only 296 cycles before it was affected by the migration of LiPSs through the PP separator, leading to large degrees of surface degradation of the electrodes and possible short-circuiting. Thus, suppression of the LiPSs and their reutilization when using an MC separator during cycling of the battery enhanced the overall capacity of the cell. We also examined the loading of c-MoS_2 required to obtain a stable capacity and CE. A higher dispersion (5 or 10 mg) affected the capacity of the battery as well as low CE. The cell assembled with a separator coated with 5 mg of the dispersion of c-MoS_2 tested at 0.5C rate provided an initial capacity of 930 mA h g^{-1} and only 82% CE after 250 cycles (Fig. S10a and b†); with 10 mg of the c-MoS_2 dispersion, the cell displayed an initial capacity of 889 mA h g^{-1}, and after the 250^{th} cycle the capacity dropped to 569 mA h g^{-1} with 79% CE (Fig. S10a and b†). We suspect that an excess of c-MoS_2 might have hindered charge transport in the LSB; alternatively, an extreme degree of physical adsorption of LiPSs might have been caused by a higher amount of c-MoS_2 not allowing stripping of adsorbed LiPSs from the surface, adding additional resistance and, ultimately, affecting the capacity and stability of the cell.[13]

We tested the electrochemical performance of cells containing the MC separator at higher C-rates. At a rate of 1C, the cell provided an initial capacity of 1034 mA h g^{-1} with 96% CE after 500 cycles (Fig. 5b). At 3C, the cell displayed an initial capacity of 930 mA h g^{-1}, with 95% CE for more than 750 cycles (Fig. S11†). At an even higher C-rate of 5C, the cell exhibited an initial capacity of 709 mA h g^{-1} and a capacity after 1800 cycles of 268 mA h g^{-1} (Fig. S12†); the CE after the 1800^{th} cycle was 88%, with the decay rate per cycle of approximately 0.034% per cycle. We then studied the reversible capacities of the cells operated at the various C-rates (Fig. 5c). At rates of 0.25, 0.5, 1, 2, 3, and 5C, the MC separator provided average capacities (from a total of eight cycles) of 1301, 1127, 1032, 973, 938, and 858 mA h g^{-1}, respectively. Upon switching the C-rate back to 0.25C, the cell displayed an average capacity of 1451 mA h g^{-1}. This higher reversible capacity can be correlated to the enhanced polysulfide conversion during the charge/discharge cycles at higher C rates. In contrast, the cell incorporating the PP separator displayed poor performance, with average capacities of 665, 556, 488, 428, 398, and 340 mA h g^{-1} at rates of 0.25, 0.5, 1, 2, 3, and 5C, respectively. Upon switching back to a rate of 0.25C, the average reversible capacity was 664 mA h g^{-1}. The GCD profiles (1^{st} cycle at each C-rate) of the cells cycled at the various C-rates revealed the reversibility of the cell capacity at 0.25C. The cell incorporating the MC separator revealed no difference in the discharge capacity when we switched the C-rate back from 5C to 0.25C (Fig. 5d). In contrast, we observed a capacity loss in the cell featuring the PP separator when switching the C-rate from 5C to 0.25C (Fig. S13†). We compared the GCD profiles of the cells at reversible 0.25C rate of the cell tested for different C rate performance to determine the conversion reaction of sulfur to LiPSs and the polarization potential (ΔE) (Fig. 5e). The GCD plateaus of the cell containing the MC separator revealed the regular conversion of long-range LiPSs to short-range LiPSs. The GCD profile of the MC separator featured two discharge plateaus that were relevant to the CV curves. The first plateau, at 2.32 V, represents the reduction of elemental sulfur to a soluble long-range polysulfide ($S_8 \rightarrow S_6^{2-} \rightarrow S_4^{2-}$);[14,18] the second, at 2.09 V, represents the further reduction of soluble LiPSs to insoluble lithium sulfide or short-

Published on 29 March 2023. Downloaded on 6/22/2024 6:17:22 AM.

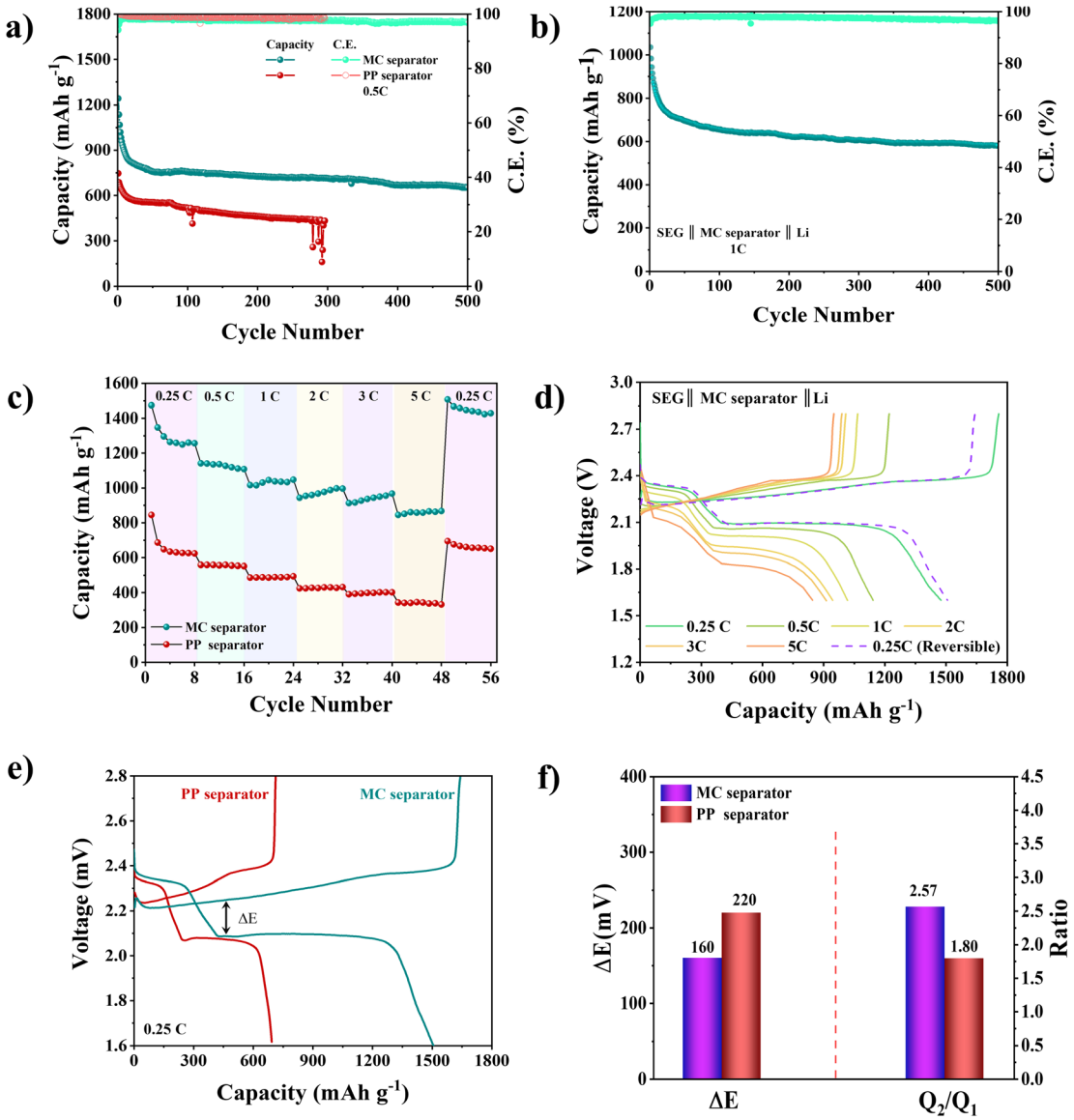

Fig. 5 Electrochemical performance and CEs of LSBs incorporating PP and MC separators, recorded at rates of (a) 0.5C and (b) 1C. (c) Electrochemical performance and reversible capacity of LSBs incorporating PP and MC separators, recorded at various C-rates. (d) GCD plateaus of LSBs incorporating MC separators, recorded at various C-rates. (e) GCD plateaus of LSBs incorporating MC separators, recorded at 0.25C ΔE. (f) Comparison of the values of ΔE and Q_2/Q_1 ratios calculated from the GCD cycles performed at a rate of 0.25C in (e).

range LiPSs ($S_4 \rightarrow Li_2S_2 \rightarrow Li_2S$).[19,50] The value of ΔE, the voltage difference between the oxidation potential and second reduction potential, for the cell incorporating the MC separator was substantially lower (160 mV) than that of the cell prepared with the PP separator (220 mV). This lower polarization potential confirms that the MC separator improved the redox kinetics of the cell. The electrochemical performance of the MC separator has been compared with other modified separators in Table S2.†

We investigated the improved catalytic activity in the cell incorporating the MC separator in terms of the Q_2/Q_1 ratio, where Q_1 and Q_2 represent the capacities at the first and second discharge plateaus, respectively. Here, a higher ratio indicates greater catalytic activity in a cell.[50] We analyzed the GCD plateaus of the cells cycled at 0.25C. Fig. 5f reveals that the Q_2/Q_1 ratio of the cell containing the MC separator (2.57) was greater than that for the cell containing the PP separator (1.80). The MC separator-containing cell, with its higher capacity ratio, demonstrated enhanced catalytic activity for the redox kinetics of the LiPSs. The 1T′-phase c-MoS_2 structure offered enhanced conductivity to the PP separator, helping to transform the LiPSs to Li_2S_x ($x = 1, 2$) and, hence, leading to enhanced and stable performance.[12] Furthermore, the high EASA and strained-sulfur vacancies on the c-MoS_2 surface boosted the effective utilization of sulfur and LiPSs, as reflected by the high performance of the LSB.

 This journal is © The Royal Society of Chemistry 2023

Published on 29 March 2023. Downloaded on 6/22/2024 6:17:22 AM.

4. Conclusion

To suppress LiPSs shuttling in LSBs, we prepared a modified separator through a simple vacuum-filtration process. LSBs assembled with a PP separator modified with c-MoS_2 nanosheets exhibited enhanced electrochemical performance. The crumpled structure of c-MoS_2 allowed it to adhere tightly to the PP separator, leading to its interlocking with the porous separator. The high EASA and strained-sulfur vacancies on the surface of the c-MoS_2 nanosheets boosted the utilization of sulfur and LiPSs. In addition, the presence of the 1T phase in the c-MoS_2 structure offered enhanced electrical conductivity, ultimately decreasing the interfacial resistance between the cathode and separator. Consequently, an H-cell demonstration and UV absorption study revealed lower degrees of infiltration of LiPSs when using the MC separator. SEM imaging of the surface morphology of the Li anode revealed that it was well protected in the cell prepared with the MC separator, relative to the situation in cell featuring the PP separator. Moreover, XPS analysis of the MC separator revealed a lower degree of migration of LiPSs on the anode. The lower polarization potential and higher Q_2/Q_1 ratio of the LSB prepared with the MC separator indicated its lower interfacial resistance and enhanced capacity, respectively. The LSB assembled with an SEG cathode, an MC separator, and a Li anode provided stable capacities when operated at rates of 0.5C, 1C, 3C, and 5C for prolonged cycles.

Author contributions

Rohan Paste: conceptualization, methodology, device fabrication and analysis, characterization and investigation, visualization, writing original draft. Shenghan Li: some characterization (electrochemical tests and surface morphology). Jui-Han Fu, Yu Hsiang Chiang: some materials synthesis and characterization. Arif I. Inamdar, Ming-Hsi Chiang: surface area and pore size distribution. Vincent Tung: supervision and funding acquisition. Hong-Cheu Lin: supervision and funding acquisition. Chih Wei Chu: conceptualization, validation, writing review and editing, supervision, funding acquisition.

Conflicts of interest

The authors declare no conflicts of interest.

Acknowledgements

Dr C. W. Chu thanks the National Science and Technology Council (NSTC), Taiwan (grant no. MOST 107-2221-E-001-007-MY3 and MOST 110-2124-M-001-001), for financial support. Prof. H.-C. Lin thanks NSTC, Taiwan (grant no. MOST 110-2221-E-A49-003-MY3, MOST 110-2113-M-A49-018, and NSTC 111-2634-F-A49-007), for financial support. This study was also supported by the Center for Emergent Functional Matter Science of National Yang Ming Chiao Tung University from The Featured Areas Research Center Program within the framework of the Higher Education Sprout Project by the Ministry of Education (MOE) in Taiwan. We thank the Advanced Materials Characterization Lab, Institute of Atomic and Molecular Sciences, Academia Sinica, Taipei, for their technical support.

References

1 G. Zhou, H. Chen and Y. Cui, *Nat. Energy*, 2022, **7**, 312–319.
2 J.-W. Park, S.-C. Jo, M.-J. Kim, I.-H. Choi, B. G. Kim, Y.-J. Lee, H.-Y. Choi, S. Kang, T. Kim and K.-J. Baeg, *NPG Asia Mater.*, 2021, **13**, 30.
3 M. Zhao, B.-Q. Li, X.-Q. Zhang, J.-Q. Huang and Q. Zhang, *ACS Cent. Sci.*, 2020, **6**, 1095–1104.
4 J. Tan, J. Matz, P. Dong, M. Ye and J. Shen, *Energy Storage Mater.*, 2021, **42**, 645–678.
5 H. Yuan, H.-J. Peng, J.-Q. Huang and Q. Zhang, *Adv. Mater. Interfaces*, 2019, **6**, 1802046.
6 T. Ould Ely, D. Kamzabek, D. Chakraborty and M. F. Doherty, *ACS Appl. Energy Mater.*, 2018, **1**, 1783–1814.
7 D.-W. Wang, Q. Zeng, G. Zhou, L. Yin, F. Li, H.-M. Cheng, I. R. Gentle and G. Q. M. Lu, *J. Mater. Chem. A*, 2013, **1**, 9382–9394.
8 H. Yuan, H.-J. Peng, B.-Q. Li, J. Xie, L. Kong, M. Zhao, X. Chen, J.-Q. Huang and Q. Zhang, *Adv. Energy Mater.*, 2019, **9**, 1802768.
9 G. Zhou, H. Tian, Y. Jin, X. Tao, B. Liu, R. Zhang, Z. W. Seh, D. Zhuo, Y. Liu, J. Sun, J. Zhao, C. Zu, D. S. Wu, Q. Zhang and Y. Cui, *Proc. Natl. Acad. Sci. U. S. A.*, 2017, **114**, 840–845.
10 A. N. Mistry and P. P. Mukherjee, *J. Phys. Chem. C*, 2018, **122**, 23845–23851.
11 J.-J. Yuan, Q.-R. Kong, Z. Huang, Y.-Z. Song, M.-Y. Li, L.-F. Fang, B.-K. Zhu and H.-Y. Li, *J. Mater. Chem. A*, 2021, **9**, 2970–2979.
12 H. Yao, K. Yan, W. Li, G. Zheng, D. Kong, Z. W. Seh, V. K. Narasimhan, Z. Liang and Y. Cui, *Energy Environ. Sci.*, 2014, **7**, 3381–3390.
13 S. Li, W. Zhang, J. Zheng, M. Lv, H. Song and L. Du, *Adv. Energy Mater.*, 2021, **11**, 2000779.
14 M. Li, D. Yang, J. J. Biendicho, X. Han, C. Zhang, K. Liu, J. Diao, J. Li, J. Wang, M. Heggen, R. E. Dunin-Borkowski, J. Wang, G. Henkelman, J. R. Morante, J. Arbiol, S.-L. Chou and A. Cabot, *Adv. Funct. Mater.*, 2022, 2200529.
15 B. He, Z. Rao, Z. Cheng, D. Liu, D. He, J. Chen, Z. Miao, L. Yuan, Z. Li and Y. Huang, *Adv. Energy Mater.*, 2021, **11**, 2003690.
16 H. Sul, A. Bhargav and A. Manthiram, *Adv. Energy Mater.*, 2022, **12**, 2200680.
17 S. Chen, Z. Song, Y. Ji, K. Yang, J. Fang, L. Wang, Z. Wang, Y. Zhao, Y. Zhao, L. Yang and F. Pan, *Small Methods*, 2021, **5**, 2100839.
18 Z. Huang, L. Wang, Y. Xu, L. Fang, H. Li, B. Zhu and Y. Song, *J. Chem. Eng.*, 2022, **443**, 136347.
19 J. Zheng, G. Ji, X. Fan, J. Chen, Q. Li, H. Wang, Y. Yang, K. C. DeMella, S. R. Raghavan and C. Wang, *Adv. Energy Mater.*, 2019, **9**, 1803774.
20 J. Zhang, Q. Rao, B. Jin, J. Lu, Q.-g. He, Y. Hou, Z. Li, X. Zhan, F. Chen and Q. Zhang, *J. Chem. Eng.*, 2020, **388**, 124120.

Published on 29 March 2023. Downloaded on 6/22/2024 6:17:22 AM.

21 F. Pei, L. Lin, A. Fu, S. Mo, D. Ou, X. Fang and N. Zheng, *Joule*, 2018, **2**, 323–336.
22 Y. Ren, B. Wang, H. Liu, H. Wu, H. Bian, Y. Ma, H. Lu, S. Tang and X. Meng, *J. Chem. Eng.*, 2022, **450**, 138046.
23 L. Luo, X. Qin, J. Wu, G. Liang, Q. Li, M. Liu, F. Kang, G. Chen and B. Li, *J. Mater. Chem. A*, 2018, **6**, 8612–8619.
24 X. Wang, L. Yang, Y. Wang, Q. Li, C. Chen, B. Zhong, Y. Chen, X. Guo, Z. Wu, Y. Liu, Y. Liu and Y. Sun, *J. Colloid Interface Sci.*, 2022, **606**, 666–676.
25 Z. A. Ghazi, X. He, A. M. Khattak, N. A. Khan, B. Liang, A. Iqbal, J. Wang, H. Sin, L. Li and Z. Tang, *Adv. Mater.*, 2017, **29**, 1606817.
26 M. Liu, C. Zhang, J. Su, X. Chen, T. Ma, T. Huang and A. Yu, *ACS Appl. Mater. Interfaces*, 2019, **11**, 20788–20795.
27 X. Yu, G. Zhou and Y. Cui, *ACS Appl. Mater. Interfaces*, 2019, **11**, 3080–3086.
28 Y.-C. Chen, A.-Y. Lu, P. Lu, X. Yang, C.-M. Jiang, M. Mariano, B. Kaehr, O. Lin, A. Taylor, I. D. Sharp, L.-J. Li, S. S. Chou and V. Tung, *Adv. Mater.*, 2017, **29**, 1703863.
29 J.-H. Fu, A.-Y. Lu, N. J. Madden, C. C. Wu, Y.-C. Chen, M.-H. Chiu, K. Hattar, J. A. Krogstad, S. S. Chou, L.-J. Li, J. Kong and V. Tung, *Commun. Mater.*, 2020, **1**, 42.
30 R. Paste, C. Hanmandlu, P.-Y. Su, C.-H. Hou, H.-A. Chen, C.-W. Pao, J.-J. Shyue, K.-H. Chen, H.-L. Wu, H.-C. Lin and C. W. Chu, *J. Chem. Eng.*, 2023, **452**, 139088.
31 K. Sun, C. Wang, Y. Dong, P. Guo, P. Cheng, Y. Fu, D. Liu, D. He, S. Das and Y. Negishi, *ACS Appl. Mater. Interfaces*, 2022, **14**, 4079–4090.
32 Z. Wang, L. Ma, W. Chen, G. Huang, D. Chen, L. Wang and J. Y. Lee, *RSC Adv.*, 2013, **3**, 21675–21684.
33 K. D. Rasamani, F. Alimohammadi and Y. Sun, *Mater. Today*, 2017, **20**, 83–91.
34 C. D. Quilty, L. M. Housel, D. C. Bock, M. R. Dunkin, L. Wang, D. M. Lutz, A. Abraham, A. M. Bruck, E. S. Takeuchi, K. J. Takeuchi and A. C. Marschilok, *ACS Appl. Energy Mater.*, 2019, **2**, 7635–7646.
35 H. R. Inta, T. Biswas, S. Ghosh, R. Kumar, S. K. Jana and V. Mahalingam, *ChemNanoMat*, 2020, **6**, 685–695.
36 A. P. Khedulkar, V. D. Dang, B. Pandit, T. Ai Ngoc Bui, H. L. Tran and R.-a. Doong, *J. Colloid Interface Sci.*, 2022, **623**, 845–855.
37 E. Cha, M. D. Patel, J. Park, J. Hwang, V. Prasad, K. Cho and W. Choi, *Nat. Nanotechnol.*, 2018, **13**, 337–344.
38 X. Gan, L. Y. S. Lee, K.-y. Wong, T. W. Lo, K. H. Ho, D. Y. Lei and H. Zhao, *ACS Appl. Energy Mater.*, 2018, **1**, 4754–4765.
39 A. I. Inamdar, N. Kaisar, S. Kamal, T.-T. Luo, S. Jou, C.-W. Chu, M.-H. Chiang and K.-L. Lu, *ChemElectroChem*, 2021, **8**, 3040–3048.
40 H. Ma, J. Liu, H. Hua, L. Peng, X. Shen, X. Wang, P. Zhang and J. Zhao, *ACS Appl. Mater. Interfaces*, 2021, **13**, 27663–27673.
41 W. Chen, T. Qian, J. Xiong, N. Xu, X. Liu, J. Liu, J. Zhou, X. Shen, T. Yang, Y. Chen and C. Yan, *Adv. Mater.*, 2017, **29**, 1605160.
42 C.-H. Chang, S.-H. Chung and A. Manthiram, *Small*, 2016, **12**, 174–179.
43 S.-H. Chung and A. Manthiram, *Adv. Funct. Mater.*, 2014, **24**, 5299–5306.
44 R. Paste, S. A. Abbas, A. Singh, H.-C. Lin and C. W. Chu, *J. Power Sources*, 2021, **507**, 230306.
45 V. Shutthanandan, M. Nandasiri, J. Zheng, M. H. Engelhard, W. Xu, S. Thevuthasan and V. Murugesan, *J. Electron Spectrosc. Relat. Phenom.*, 2019, **231**, 2–10.
46 M. J. Lacey, A. Yalamanchili, J. Maibach, C. Tengstedt, K. Edström and D. Brandell, *RSC Adv.*, 2016, **6**, 3632–3641.
47 M. I. Nandasiri, L. E. Camacho-Forero, A. M. Schwarz, V. Shutthanandan, S. Thevuthasan, P. B. Balbuena, K. T. Mueller and V. Murugesan, *Chem. Mater.*, 2017, **29**, 4728–4737.
48 X. Lv, W. Guo, J. Song and Y. Fu, *Small*, 2022, **18**, 2105071.
49 Y. Yang, G. Yu, J. J. Cha, H. Wu, M. Vosgueritchian, Y. Yao, Z. Bao and Y. Cui, *ACS Nano*, 2011, **5**, 9187–9193.
50 Z. Liang, D. Yang, P. Tang, C. Zhang, J. J. Biendicho, Y. Zhang, J. Llorca, X. Wang, J. Li, M. Heggen, J. David, R. E. Dunin-Borkowski, Y. Zhou, J. R. Morante, A. Cabot and J. Arbiol, *Adv. Energy Mater.*, 2021, **11**, 2003507.

 This journal is © The Royal Society of Chemistry 2023